The Plasma Factor XIII Heterotetrameric Complex Structure: Unexpected Unequal Pairing within a Symmetric Complex

Sneha Singh, Alexis Nazabal, Senthilvelrajan Kaniyappan, Jean-Luc Pellequer, Alisa Wolberg, Diana Imhof, Johannes Oldenburg, Arijit Biswas

biomolecules

MDPI

Article

The Plasma Factor XIII Heterotetrameric Complex Structure: Unexpected Unequal Pairing within a Symmetric Complex

Sneha Singh [1], Alexis Nazabal [2], Senthilvelrajan Kaniyappan [3], Jean-Luc Pellequer [4], Alisa S. Wolberg [5], Diana Imhof [6], Johannes Oldenburg [1] and Arijit Biswas [1,*]

1 Institute of Experimental Hematology and Transfusion medicine, University Hospital of Bonn, Sigmund-Freud Street 25, 53127 Bonn, Germany; Sneha.Gupta@ukbonn.de (S.S.); Johannes.Oldenburg@ukbonn.de (J.O.)
2 CovalX, Schützengasse 2, CH-8001 Zürich, Switzerland; alexis.nazabal@covalx.com
3 German Center for Neurodegenerative Diseases (DZNE), Sigmund-Freud-Str. 27, 53127 Bonn, Germany; Senthil.Kaniyappan@dzne.de
4 Univ. Grenoble Alpes, CEA, CNRS, IBS, F-38000 Grenoble, France; jean-luc.pellequer@ibs.fr
5 Department of Pathology and Laboratory Medicine and UNC Blood Research Center, University of North Carolina at Chapel Hill, 8018A Mary Ellen Jones Building, Chapel Hill, NC 27599-7035, USA; alisa_wolberg@med.unc.edu
6 Pharmaceutical Biochemistry and Bioanalytics, Pharmaceutical Institute, University of Bonn, An der Immenburg 4, 53121 Bonn, Germany; dimhof@uni-bonn.de
* Correspondence: arijit.biswas@ukb.uni-bonn.de; Tel.: +49-228-2871-9428; Fax: +49-228-2871-6087

Received: 25 October 2019; Accepted: 19 November 2019; Published: 21 November 2019

Abstract: Factor XIII (FXIII) is a predominant determinant of clot stability, strength, and composition. Plasma FXIII circulates as a pro-transglutaminase with two catalytic A subunits and two carrier-protective B subunits in a heterotetramer (FXIII-A_2B_2). FXIII-A_2 and -B_2 subunits are synthesized separately and then assembled in plasma. Following proteolytic activation by thrombin and calcium-mediated dissociation of the B subunits, activated FXIII (FXIIIa) covalently cross links fibrin, promoting clot stability. The zymogen and active states of the FXIII-A subunits have been structurally characterized; however, the structure of FXIII-B subunits and the FXIII-A_2B_2 complex have remained elusive. Using integrative hybrid approaches including atomic force microscopy, cross-linking mass spectrometry, and computational approaches, we have constructed the first all-atom model of the FXIII-A_2B_2 complex. We also used molecular dynamics simulations in combination with isothermal titration calorimetry to characterize FXIII-A_2B_2 assembly, activation, and dissociation. Our data reveal unequal pairing of individual subunit monomers in an otherwise symmetric complex, and suggest this unusual structure is critical for both assembly and activation of this complex. Our findings enhance understanding of mechanisms associating FXIII-A_2B_2 mutations with disease and have important implications for the rational design of molecules to alter FXIII assembly or activity to reduce bleeding and thrombotic complications.

Keywords: coagulation factor XIII complex; threaded modeling; cross-linking mass spectrometry; HADDOCK flexible docking; molecular dynamics simulation; atomic force microscopy; isothermal titration calorimetry

1. Introduction

Plasma coagulation factor XIII (FXIII) circulates as a heterotetramer composed of two catalytic FXIII-A subunits tightly-associated (10^{-7}–10^{-9} M) with two carrier/regulatory FXIII-B subunits

(FXIII-A_2B_2) [1,2]. During coagulation, proteolytic activation by thrombin and calcium-mediated dissociation of FXIII-B subunit generates activated FXIII-A (FXIIIa) that covalently cross links fibrin, promoting clot stability [3]. Deficiency in plasma FXIII antigen or activity is associated with mild-to-severe bleeding [3]. The structure of the catalytic FXIII-A subunits is well-characterized, consisting of an activation peptide (FXIII-AP, residues 1–37) followed by four distinct domains: β-sandwich (residues 38–183), central core (residues 184–515), β-barrel-1 (residues 516–627), and β-barrel-2 (residues 628–731) [4]. Both zymogen and activated forms of FXIII-A have been crystallized [4,5], revealing a compact structure of zymogen FXIII-A_2, but an open, extended conformation of activated FXIIIa. Despite the essential regulatory role of FXIII-B, structural information on this molecule is sparse. Sequence homology with complement proteins suggest each FXIII-B subunit is composed of ten sushi domains, each containing ~60 amino acid residues and two disulfide bonds [6]. Although sedimentation analysis initially suggested FXIII-B is a monomer, more recent data suggest FXIII-B circulates as a dimer [6,7]. Sushi domains 4 and 9 (S4 and S9) are thought to mediate FXIII-B_2 dimerization, whereas S1 and S2 are thought to promote interactions with the FXIII-A subunits [1,6]. The size and complexity of FXIII-A_2B_2 make it difficult to characterize by traditional methods such as X-ray crystallography or NMR. Apart from a partial all-atom model generated with minimal experimental data [8], there is no detailed model for the FXIII-B_2 dimer or the FXIII-A_2B_2 complex. Consequently, knowledge of the structural interface between FXIII-B subunits or the FXIII-A_2B_2 heterotetramer is incomplete. Structural resolution of plasma FXIII-A_2B_2 and its transition to activated FXIIIa is essential for defining implications of missense FXIII mutations, as well as the development of potential FXIII(a) inhibitors for treating bleeding and thrombotic complications associated with abnormal clot stabilization

Integrative/hybrid (IH) approaches are useful for dissecting the structural architecture of complexes that escape traditional structural determination techniques [9,10]. These approaches integrate biochemical and computed data to yield structural information on macromolecular complexes. For example, IH has revealed detailed molecular conformational states of glucagon receptor [11] and the chromatin remodeling complex [12], and recently a combination of structural methods with atomic force microscopy (AFM) has provided key information on factor Va bound to activated protein C [13]. Since FXIII-A_2B_2 has not been amenable to traditional structural analysis, we addressed this gap using a bootstrapped IH approach. We first used atomic force microscopy to define the macromolecular structure of the FXIII subunits individually and as a complex, and chemical cross-linking and mass spectrometry (XL-MS) to define residues in the FXIII-A_2B_2 inter-subunit interface. We then used these data as structural constraints to assemble, first, a monomeric FXIII-B subunit model followed by an all-atom structural model of the FXIII-A_2B_2 complex. We then overlaid these putative models on surface topographic atomic force micrographs of FXIII-A_2B_2 to produce a complete macromolecular structure [10]. Finally, we integrated molecular simulations from the all-atom model with ITC (isothermal titration calorimetry) to interrogate conformational thermodynamics during FXIII-A_2B_2 assembly, activation, and subunit disassociation. Our data indicate FXIII-A_2B_2 assembles with unexpected unequal pairing within an otherwise symmetric complex, and suggest this conformation is essential for FXIII function. These findings provide the first molecular structure of this important coagulation protein.

2. Materials and Methods

Software, databases, and webservers used in this study are listed in Supplementary Table S1. A flowchart for the IH approach is presented in Supplementary Figure S1 [14,15]. The PDB co-ordinates for one of the simulation snapshots of the complex model taken from the production phase of the simulation trajectory is provided as a supplementary file. Detailed methodology can be found in the Supplementary Methods.

2.1. FXIII-A and FXIII-B Subunit, Cloning Expression, and Purification

Cloning expression and purification of rFXIII-A (recombinant FXIII-A) subunit was performed as described by Gupta et al., 2016 [8] (Supplementary Figure S2a). Human FXIII-B cDNA, inserted into the cloning site of pReciever-M01 mammalian expression vector, was transfected into HEK293t cells, as per previously reported protocol [16]. Secreted protein harvested post-transfection was concentrated and subjected to immunoaffinity purification using the Thermo Scientific Pierce Co-IP kit (Pierce Biotechnology, USA) (Supplementary Figure S2b).

2.2. Purification of FXIII-A_2B_2 Complex

FibrogamminP (CSL Behring, Germany) reconstituted in water was run on a Superdex 200 increase 10/300 column /Äkta Pure system (GE healthcare, Germany) equilibrated with 20 mM Tris and 100 mM NaCl, at pH 7.4. The peak corresponding to FXIII-A_2B_2 (320 Kda) was repurified in triplicate, until a highly pure, single, homogenous, monodispersed peak was obtained with no excipients (Supplementary Figure S2c). The eluted peak was concentrated and quantified for further downstream applications.

2.3. Atomic Force Microscopy (AFM) of FXIII

Surface topology of recombinant FXIII-A_2 (rFXIII-A_2 expressed and purified in-house), recombinant FXIII-B_2 (rFXIII-B_2 expressed and purified in-house), and FXIII-A_2B_2 (purified from FibrogamminP, CSL Behring, Marburg, Germany) was analyzed individually using high-resolution AFM. Briefly, samples suspended in PBS pH 7.4 (1–2 mM) were placed on a freshly-cleaved mica and allowed to adsorb (15 min). Non-adherent proteins were removed by washing twice with imaging buffer (10 mM Tris-HCl, 50 mM KCl, pH 7.4). Samples were imaged in oscillation mode in liquid (imaging buffer) as described *by [17]* and acquired using a Nanoscope III microscope.

2.4. XL-MS of FXIII-A_2B_2 Heterotetramer Complex

One µL of 3.12 µg/mL purified FXIII-A_2B_2 was mixed with 1 µL of a matrix of re-crystallized sinapinic acid (10 mg/mL) in acetonitrile/water (1:1, *v*/*v*), triflouroacetic acid (TFA) 0.1% (K200 MALDI Kit; CovalX, Zurich, Switzerland). After mixing, 1 µL of each sample was spotted on the MALDI plate. After crystallization at room temperature, the plate was introduced in the MALDI mass spectrometer (Ultraflex III MALDI ToF, Bruker Daltonik GmbH, Bremen, Germany) equipped with HM2 high-mass detection (CovalX, Zurich, Switzerland) and analyzed immediately in high-mass MALDI mode. MS data were analyzed using Complex Tracker analysis software (CovalX, Zurich, Switzerland). For characterization and peptide mass fingerprinting, the purified FXIII-A_2B_2 complex was subjected to ASP-N, trypsin, chymotrypsin, elastase, and thermolysin proteolysis, followed by nLC-LTQ Orbitrap MS/MS analysis (formic acid 1% added to the final solution after digestion) (Supplementary Figure S3). Purified FXIII-A_2B_2 (1.25 µM) was cross linked with 2 µL of DSS (d0d12) reagent (Creative Molecules Inc., Canada) at room temperature for 3 h, prior to digestion. Nano-LC chromatography was performed using an Ultimate 3000 (Dionex, IL, USA) system in-line with an LTQ Orbitrap XL mass spectrometer (ThermoFischer Scientific, IL, USA). Acquired data were analyzed by XQuest version 2.0 and Stavrox version 2.1. The FXIII-B intra-subunit and FXIII-A-FXIII-B inter-subunit cross-linked peptides and residues are presented in Supplementary Tables S2 and S3.

2.5. Generation of the FXIII-B Subunit Model

FXIII-B intra-subunit XL-MS cross-linked residues were matched to residue contact prediction data to generate constrained models of FXIII-B monomers on the AIDA server (http://aida.godziklab.org/) [18] (Supplementary Figures S4 and S5). Sushi domains were based on previously-generated high-quality threaded models from I-TASSER [19] (https://zhanglab.ccmb.med.umich.edu/I-TASSER/ (Supplementary Figure S6a–S6j). We also assembled a FXIII-B subunit monomer model (Supplementary

Figure S5) in default mode, i.e., without constraints and docked this model symmetrically (M-Z docking server [20]) to model unbound FXIII-B_2 dimer.

2.6. Generation of the FXIII-A_2B_2 All-Atom Model

Inter-subunit, XL-MS-directed docking of all FXIII-B monomer conformations on the FXIII-A_2 crystal structure (PDB ID: 1f13) was performed using the HADDOCK expert interface webserver (http://milou.science.uu.nl/services/HADDOCK2.2/) [21]. Since this webserver allows for only bi-molecular docking, whereas the in-silico model involves three proteins (FXIII-B monomer and FXIII-A_2 dimer), we treated the dimer as a single molecule by renumbering the residues of each FXIII-A monomer in continuum. We based structural constraints for modeling and docking FXIII-B monomer on FXIII-A_2 on inter- and intra-subunit cross-linked residues (Supplementary Tables S2 and S3). Docking constraints (n = 64) required that all residues belong to detected cross-linked peptides that can form side chain contacts (Supplementary Table S4) to cover the FXIII-A_2/FXIII-B trimer surface. Moreover, FXIII-A_2/FXIII-B contact residues were assigned constant lower and upper limit distances of 3 and 24 Å, respectively [22]. We then manually constructed the resulting docked trimer into a tetramer with bilateral symmetry.

2.7. Molecular Dynamics Simulations of the FXIII-A_2B_2 Heterotetramer Models

Stability of the top-scoring FXIII-A_2B_2 complex (best HADDOCK scores amongst the major docking clusters, Supplementary Figure S7) from the HADDOCK [23] server was assessed using all-atom molecular dynamics (MD) simulations (YASARA Structure suite 17.4.17 platform [21,23,24] with the embedded md_sim macro) [25,26]. A steered molecular dynamics (SMD) simulation was separately performed on the MD-equilibrated model 1 to dissociate the FXIII-B_2 subunit dimer from the FXIII-A_2 dimer. The SMD was performed with md_runsteered macro embedded in YASARA, with minor modifications in the steering force (applied acceleration, 100 pm/ps^2). Analyses of simulation variables, model quality, and model characteristics are detailed in Supplementary material. All subsequent structural analyses were performed on the MD-equilibrated complex model 1.

2.8. Modeling Transition States between the First FXIII-A_2: FXIII-B_2 Contacts and the Final FXIII-A_2B_2 Complex

To generate a model of the initial contact between dimeric FXIII-A_2 and FXIII-B_2, we docked the crystal structure of FXIII-A_2 dimer with the dimeric model of unbound FXIII-B_2 on the Z-dock rigid docking server [27]. We considered the highest scoring complex as the initial contact structure and the FXIII-A_2B_2 complex model 1 generated on HADDOCK [21,23,24] as the final structure, and submitted these to the MINACTION path server (http://lorentz.dynstr.pasteur.fr/suny/submit.php?id0=minactionpath#submit) to generate C_α-backbone models of the transition-states between these two structures [28]. Once a large number of coarse-grained intermediates were generated, we converted 8 intermediates to full atom models, as described [4].

2.9. Fitting and Docking Atomic Protein Structures on AFM Surface Topographs

We docked three-dimensional heterotetramer coordinates within the AFM-derived topographic surface (envelope) using the AFM-Assembly protocol [29,30]. We defined the docking score as the number of atoms from the protein structure in the favorable layer, and translated this score into pseudo-energy values, where the best score corresponds to the lowest energy. We ran docking protocols on HADDOCK top-scored FXIII complex models, as well as on the crystal structure of FXIII-A_2 and the models of unbound FXIII-B_2. For each docking simulation, we retained the top 10^5 potential solutions and further analyzed the top 10 to produce the minimum docking energy, average energy of the top 10 docking solutions, root-mean-square deviation (RMSD) of the top 3 docking solutions, and shift of the best docking solution from the center of the docking grid.

2.10. ITC-Based Thermodynamic Profiling of the Assembly and Dissociation of the FXIII-A_2B_2 Heterotetramer Complex

Finally, we directly measured thermodynamic changes during complex assembly and disassembly of the FXIII-A_2B_2 heterotetramer using ITC on a MicroCal200 microcalorimeter (Malvern Panalyticals, Malvern, UK). To examine FXIII subunit association, we titrated 2.5 μM of rFXIII-A_2 (cell) against 25 μM rFXIII-B (syringe). We analyzed the resulting isotherms using Origin 7.0 (Originlab) and fitted the data using Affinimeter and a custom model based on stepwise association of the subunits, FS ↔ MA + A1↔MA2, where FS is free species, M is FXIII-A_2 in cell, and A is FXIII-B from syringe. To examine FXIII-A_2B_2 complex disassembly, we titrated 1.25 mM FXIII-A_2B_2 in the cell (13.8 U Thrombin; Sigma-Aldrich Chemie GmbH, Taufkirchen, Germany) against 25 mM $CaCl_2$ in the syringe. We performed blank experiments to account for the heat of dilution. We first analyzed data for a single set of binding models using Origin software, to observe binding as a global fit. We then calculated heat capacity changes for each injection based on algorithms within the Origin software and stoichiometric equilibria model (described below) in Affinimeter (https://www.affinimeter.com) and iterated between these until no further significant improvement in fit was observed. Data were fit using the custom design model and hypothetical equation M1 + A1⇋M1A1 + A1⇋M1A2 + A1⇋M1A3, where M is FXIII-A_2B_2 and A is calcium ion.

3. Results

3.1. AFM Topographs Indicates Complex Formation Restricts the Conformational Flexibility of FXIII-B

AFM analysis of the FXIII-A_2B_2 complex revealed that each isolated surface height signal had a bi-partite appearance (Supplementary Figure S8) comprised of a clearly compact part (FXIII-A subunit) from which filamentous signals (FXIII-B subunit) extended in different directions (Figure 1). The maximum height observed in the topographic images (raw) for the FXIII-A_2B_2 complex was 5.9 nm for whole field, which was lower than those recorded for either the FXIII-A_2 subunit (9.5 nm) or the FXIII-B_2 subunit (19.2 nm) (Figure 1, Supplementary Figure S8). This demonstrates that the association of FXIII-B_2 with FXIII-A_2 restricts the conformational flexibility of free FXIII-B_2 subunit making it more compact. In the surface topographic images only, part of the dispersed flexible region, i.e., the FXIII-B subunit is visible peeking out from underneath the compact part, i.e., the FXIII-A subunit. This can be explained by an overall negative charge carried by FXIII-A_2 dimer surface, which relies on positive electrostatic patches on the FXIII-B subunit to adhere to the mica surface in a complexed state (Figure 1). The differences in height might be attributed to adsorption effects on the structure of the protein [31,32]. Wrapping of FXIII-B subunits around FXIII-A_2 dimer occurred from one side, giving the molecule a bi-partite appearance, suggesting partial asymmetry in the complex.

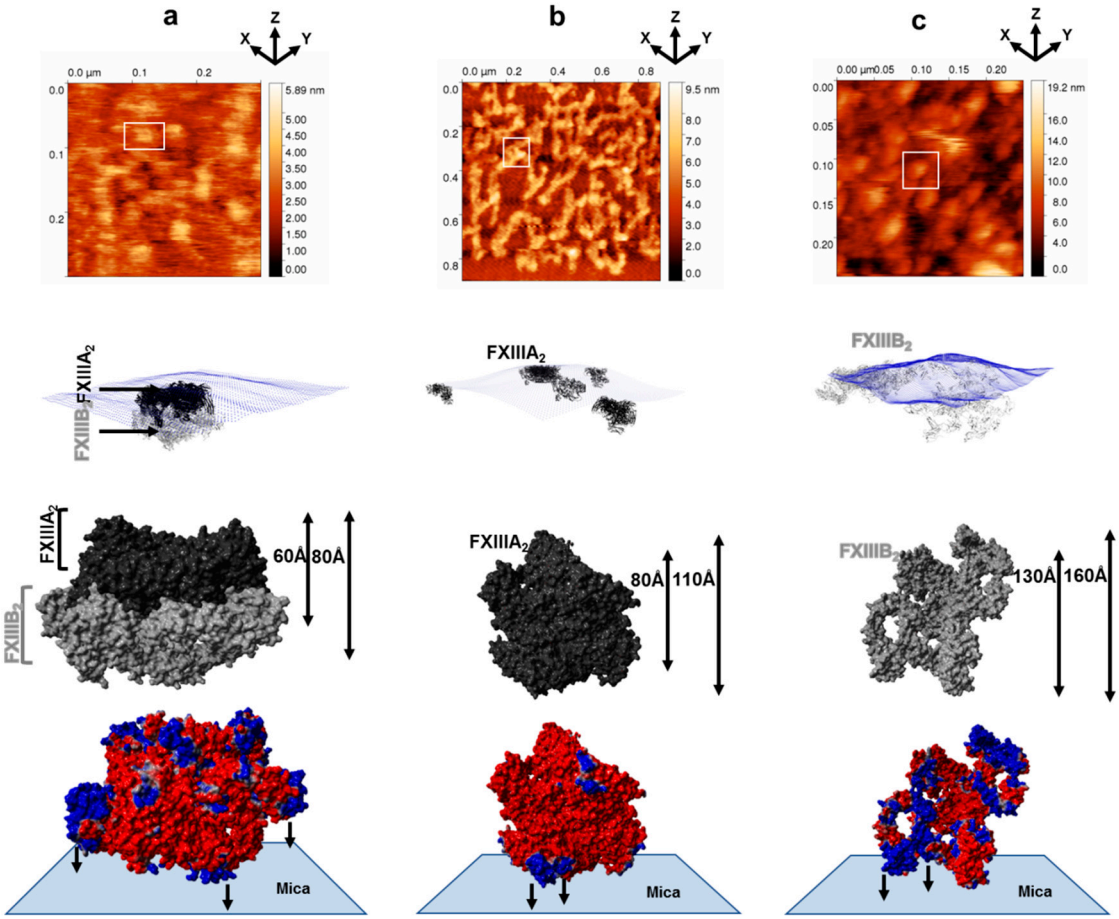

Figure 1. Conformational state of factor XIII (FXIII) complex, FXIII-A, and FXIII-B subunits by atomic force microscopy (AFM). Figure 1 is split row wise into panels a, b, and c running top to bottom. (**a**) goes top to bottom in the following order for the AFM- and AFM-based docking of the best FXIII-A_2B_2 complex model, i.e., the topmost image is the raw AFM image with the docking pose of one of the crops below it. In the docking pose, the topography is depicted as blue dots while the different docked complexes (of model one only) are depicted in black (FXIII-A_2) and gray (FXIII-B_2) ribbon format. Below the docking pose is a molecular surface-based representation of FXIII-A_2B_2 complex as it would be viewed in one of the many poses it would adopt while adhering to the mica in the AFM instrument. The minimum and maximum heights that this pose is likely to have, are indicated to the right. The FXIII-A and FXIII-B subunits are depicted in black and gray color, respectively. The lowermost image is PME electrostatic surface structural representation of the same pose depicted in alignment with the hypothetical mica surface to which it adheres. (**b**,**c**) panels follow the same trend as (**a**), only they represent the FXIII-A dimeric crystal structure and the dimeric unbound FXIII-B model, respectively.

3.2. Cross-Links in the FXIII-A_2B_2 Complex Interface Expose Reverse, N-to C-Terminal Symmetry between FXIII-A and FXIII-B Subunits

We then used XL-MS to identify inter- and intra-molecular contacts within the FXIII-A_2B_2 complex. This analysis generated 358 total peptides, with an overall coverage of 80% for FXIII-A and 91% for FXIII-B. The cross-linked FXIII-A_2B_2 heterotetramer (MW 319.950 kDa) had 34 cross-linked peptides located within the heterotetramer interface (Supplementary Table S3). Inter-subunit cross-links were detected between residues from the FXIII-A C-terminal barrel domains and the FXIII-B N-terminal S1, S2, and S3 sushi domains, whereas residues in the FXIII-A N-terminal β-sandwich domain were cross linked to residues from the FXIII-B C-terminal S6, S7, S8, and S9 sushi domains (Figure 2a). The FXIII-A catalytic core region was cross linked to FXIII-B sushi domains S3, S4, S5, S7, S8, and S9. Intra-subunit

cross-links with the FXIII-B_2 dimer interface largely involved residues in the N-terminal sushi domains (S1-S4), but fewer cross-linkings within sushi domains S6, S7, and S8 (Figure 2b, Supplementary Table S3). These findings differ from those previously reported for inter- and intra-subunit interactions within the FXIII-A_2B_2 complex [1,6].

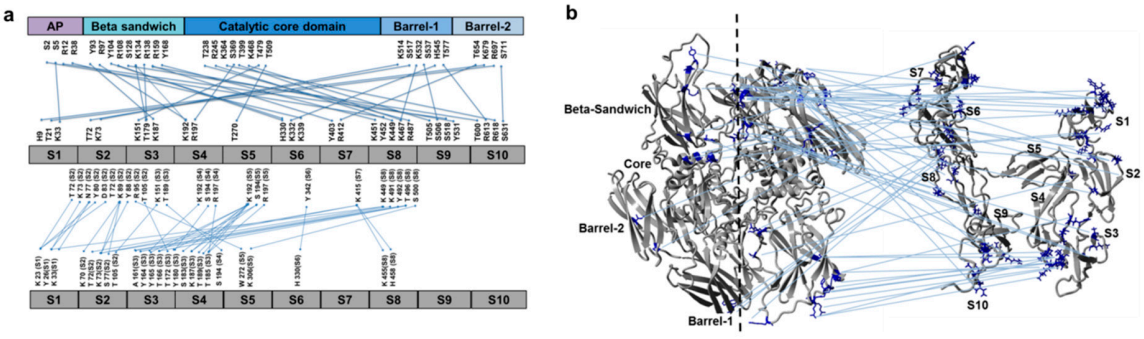

Figure 2. Cross-linking and mass spectrometry (XL-MS) derived cross-linking residues of FXIII complex reveals an N-to C-terminal symmetry. (**a**) shows the domain-wise distribution of both FXIII-B monomer model docking to FXIII-A_2 crystal structure, distance constraints (upper part of image), and monomer FXIII-B model assembly, distance constraints (lower part of image), that were generated from the XL-MS cross-linking information of the purified FXIII-A_2B_2 heterotetramer complex (Supplementary Tables S2 and S3). (**b**) shows a structural description of the information shown in (**a**). The crystal structure of the FXIII-A subunit dimer and the monomer model of the FXIII-B subunit have been illustrated in ribbon format.

3.3. Molecular Docking Reveals a Stoichiometrically-Symmetrical, Bi-Partite, FXIII-A_2B_2 Complex

To understand the origin of the reverse symmetry of the FXIII-A_2B_2 complex observed in the XL-MS data, we used molecular docking to model FXIII-A_2B_2 assembly. Of five potential models of FXIII-B monomer (Supplementary Figure S5), only two gave successfully docked clusters with FXIII-A_2; of these, we selected the topmost model (Supplementary Figure S9, chosen based on HADDOCK scores) of the top-most docking cluster as our model of choice based on agreement with structural information from AFM. This model (model 1) also illustrated a symmetric bi-partite structure, in which FXIII-A subunits are compact, and FXIII-B subunits are more dispersed and flexible (Figure 3a). Following equilibration, backbone RMSD/total energy charts (Figure 3b) indicated this model of FXIII-A_2B_2 showed good stability and was stereochemically validated (Supplementary Figure S10). Discrepancies in validation were like those observed for standard complex crystal structures. The FXIII-B N-terminal sushi domains (S1, S2, and S3 domains) extended into flexible arms (Figure 3c), although each FXIII-B monomer showed different flexibility and secondary structure following the simulation (Figure 3d,e, Supplementary video S1). We observed two distinct positively-charged electrostatic patches (two one each monomer, four in all) on FXIII-B (Figure 3f,g), which may represent potential fibrinogen interaction interfaces [33], since these would create excellent complementarity with the negatively charged regions within the currently-proposed FXIII-B interaction site on fibrinogen [33–37].

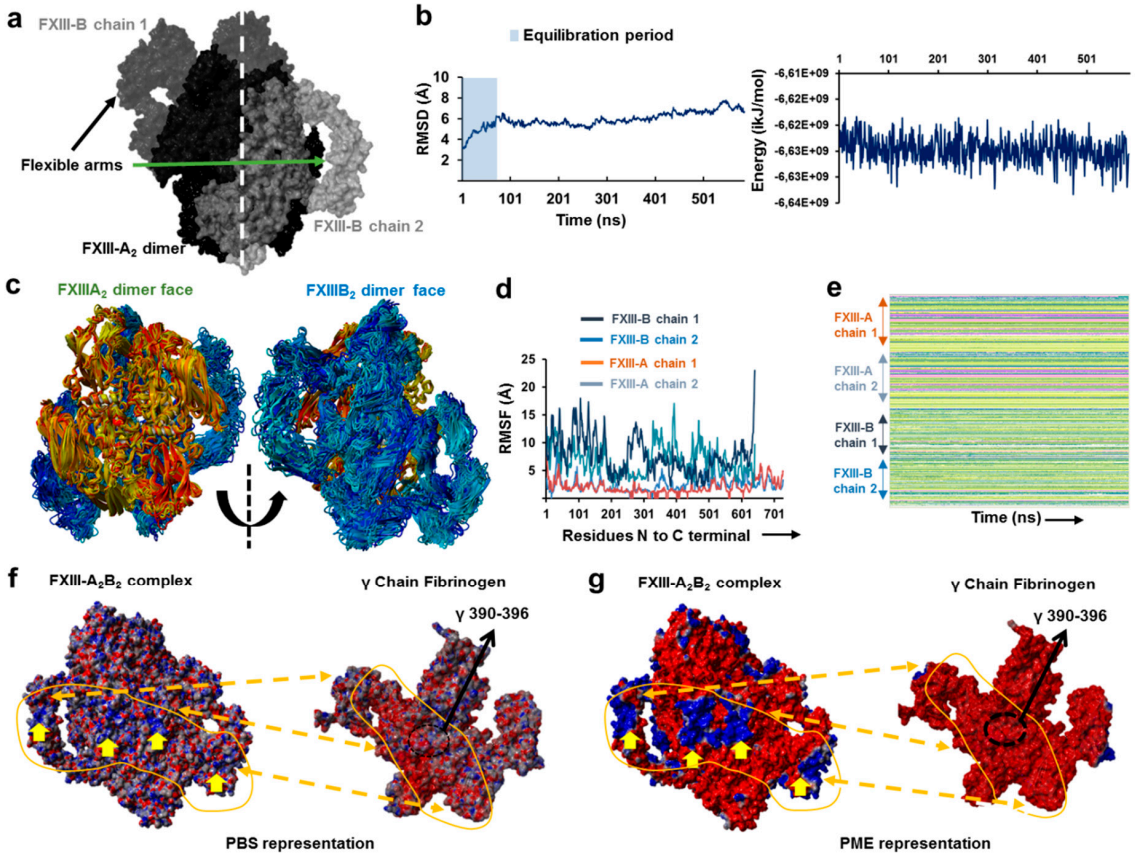

Figure 3. The all-atom structure of the FXIII-A_2B_2 complex. (**a**) is the symmetrical representation of the best modeled all-atom structure of the FXIII-A_2B_2 complex. The structure has been depicted by its molecular surface in different shades of black and gray for the individual chains of FXIII-A and FXIII-B subunits. (**b**) shows the C-α backbone RMSD and the total energy graphs for the MD simulation conducted on the FXIII-A_2B_2 complex structure model. (**c**) are aligned simulation snapshots from the MD simulation conducted on FXIII-A_2B_2 complex structure represented with FXIII-A subunit face (left) and the FXIII-B subunit face (right). The snapshots of FXIII-A and FXIII-B subunits are depicted in ribbon format with colors ranging between yellow-red and cyan-blue for either subunit, respectively. (**d**) shows the graph representing RMSF for the FXIII-A_2B_2 complex structure MD simulation, with individual chains represented by different color as mentioned in the inset. (**e**) represents the secondary structure profile of individual chains of FXIII-A and FXIII-B subunits for the FXIII-A_2B_2 complex structure MD simulation. (**f**) is the PBS-based electrostatic surface representation of the FXIII-A_2B_2 complex structure (left) and γ chain of fibrinogen (right) taken from fibrinogen crystal structure (PDB ID: 3GHG). Red color indicates negative surface electrostatic potential, whereas blue represents positive potential. Indicated positive electrostatic patches on the FXIII-A_2B_2 complex structure are likely to interact with negatively charge bearing regions in and around the FXIII interaction site of fibrinogen γ chain (the specific residues are numbered and indicated with a black arrow). (**g**) is the same view as (**f**) but electrostatic surface representation has been done with the PME method. The prominent electrostatic patches on the FXIII-B subunit are marked with yellow arrows in (**f**,**g**). The complementary electrostatic regions between FXIII and fibrinogen γ chain have been marked with dotted arrows and continuous uneven lines covering the shape of the region in (**f**,**g**).

3.4. Molecular Docking into the AFM Topographs Identifies the Best Model Representative of the Native FXIII Complex

To rule out false positive conformational models of the FXIII-A_2B_2 complex, we docked the two FXIII-A_2B_2 modeled structures onto the AFM topography image. According to the docking scores (AFM dock), FXIII-A_2B_2 complex model 1 had globally better scores than complex model 2 for the

10 selected docked regions of the AFM images (Figure 4). Each isolated surface height signal had a bi-partite appearance (Supplementary Figure S8) comprised of a compact part (FXIII-A_2) from which filamentous signals (FXIII-B) extended in different directions. The AFM topographs were in line with the complex model 1 appearance. The complex model 1, therefore, represents the native conformation of FXIII complex.

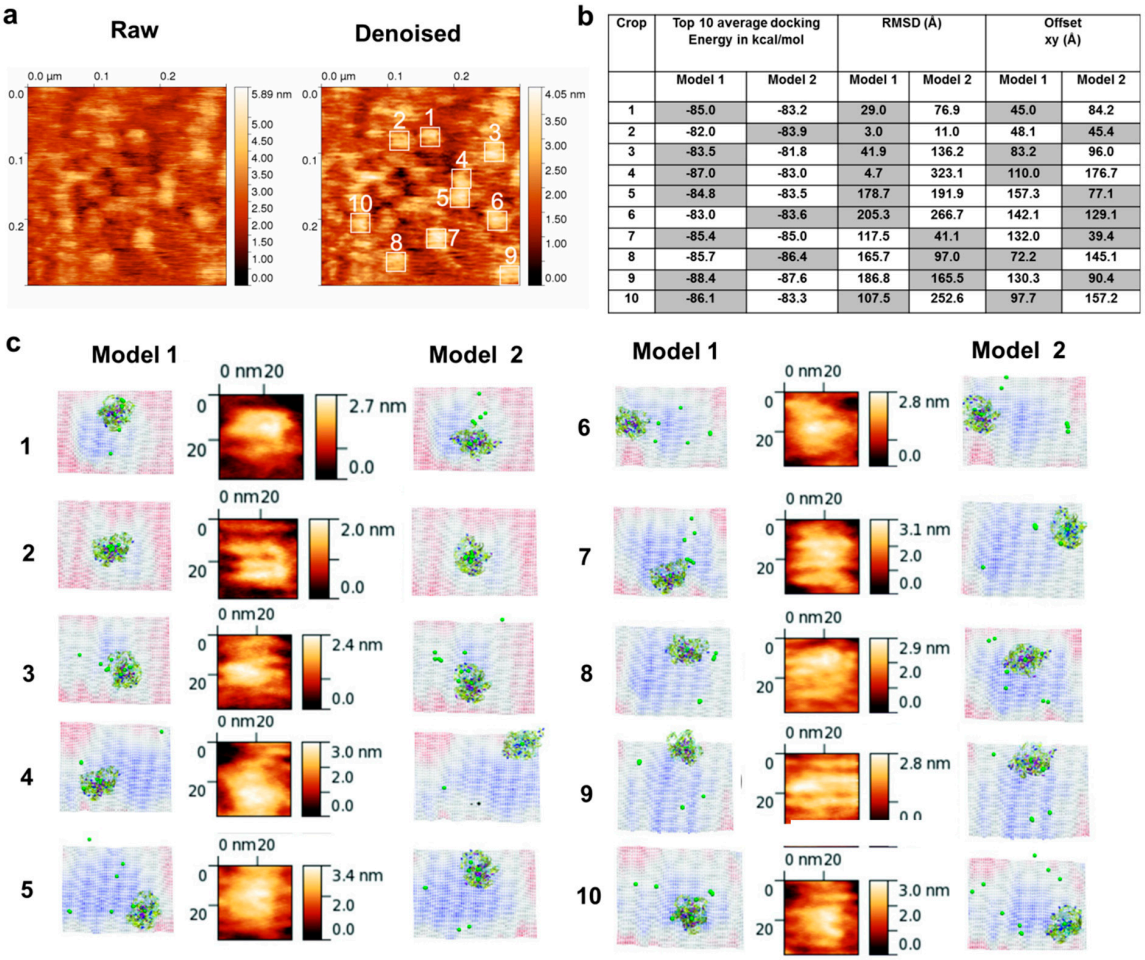

Crop	Top 10 average docking Energy in kcal/mol		RMSD (Å)		Offset xy (Å)	
	Model 1	Model 2	Model 1	Model 2	Model 1	Model 2
1	-85.0	-83.2	29.0	76.9	45.0	84.2
2	-82.0	-83.9	3.0	11.0	48.1	45.4
3	-83.5	-81.8	41.9	136.2	83.2	96.0
4	-87.0	-83.0	4.7	323.1	110.0	176.7
5	-84.8	-83.5	178.7	191.9	157.3	77.1
6	-83.0	-83.6	205.3	266.7	142.1	129.1
7	-85.4	-85.0	117.5	41.1	132.0	39.4
8	-85.7	-86.4	165.7	97.0	72.2	145.1
9	-88.4	-87.6	186.8	165.5	130.3	90.4
10	-86.1	-83.3	107.5	252.6	97.7	157.2

Figure 4. AFM based docking of FXIII complex models reveals model 1 as the best complex. (**a**) shows the raw and denoised AFM topographic images for the purified FXIII-A_2B_2 complex. The height scales are depicted to their right. The denoised image also shows in white lined squares the crops on the topographic surface to which docking of the two best models (HADDOCK scores) of the FXIII-A_2B_2 complex were performed on the DockAFM pipeline [30]. (**b**) is a table presenting the comparative scores obtained from the docking of the two FXIII-A_2B_2 complex model structures on the ten AFM image crops depicted in (**a**). The xy (offset) represents the shift of the docked model structure (model 1 and model 2) from the center of the topographic surface. The most favorable structure is chosen as that having the smallest shift from the center. (**c**) shows side-by-side the best docking pose for the two FXIII-A_2B_2 complex model structures on each of the ten crops side by side to a close-up topographic view of the crop itself. The topography of the docked pose is inverted, i.e., looking from below the surface. The color of the topography (blue to red) is the height in Z (red is low and blue is high). The structures of the two models are depicted in ribbon format.

3.5. Unequal Pairing within the Bi-Partite FXIII-A_2B_2 Complex Influences Dissociation of Subunits during FXIII Activation

Analysis of the final model 1 of the FXIII-A_2B_2 complex indicated inequality in binding of individual FXIII-B monomers to the FXIII-A_2 dimer (Figure 5a), as well as comparative differences in

pseudo-binding energies (from both simulation and PRODIGY calculations) [38] calculated for FXIII-B monomers and FXIII-A_2 subunits (Figure 5b,c). The SMD-based separation of FXIII-B_2 from FXIII-A_2 showed that even though steering force was only applied to FXIII-B, it displaced one of the FXIII-A monomers, resulting in a FXIII-A_2B heterotrimer-like scenario (Supplementary video S2). Unequal pairing results in disproportionate displacement of FXIII-A subunits, wherein strong affinity between FXIII-A and FXIII-B subunits causes the FXIII-A subunits to be pulled apart along with the FXIII-B subunit. This observation raises the possibility that a FXIII-AB heterodimer is generated transiently during activation-induced disassembly of the complex. Thus, unequal pairing of FXIII subunits results in a previously unrecognized dissociation pattern of FXIII-B and -A subunits during FXIII activation.

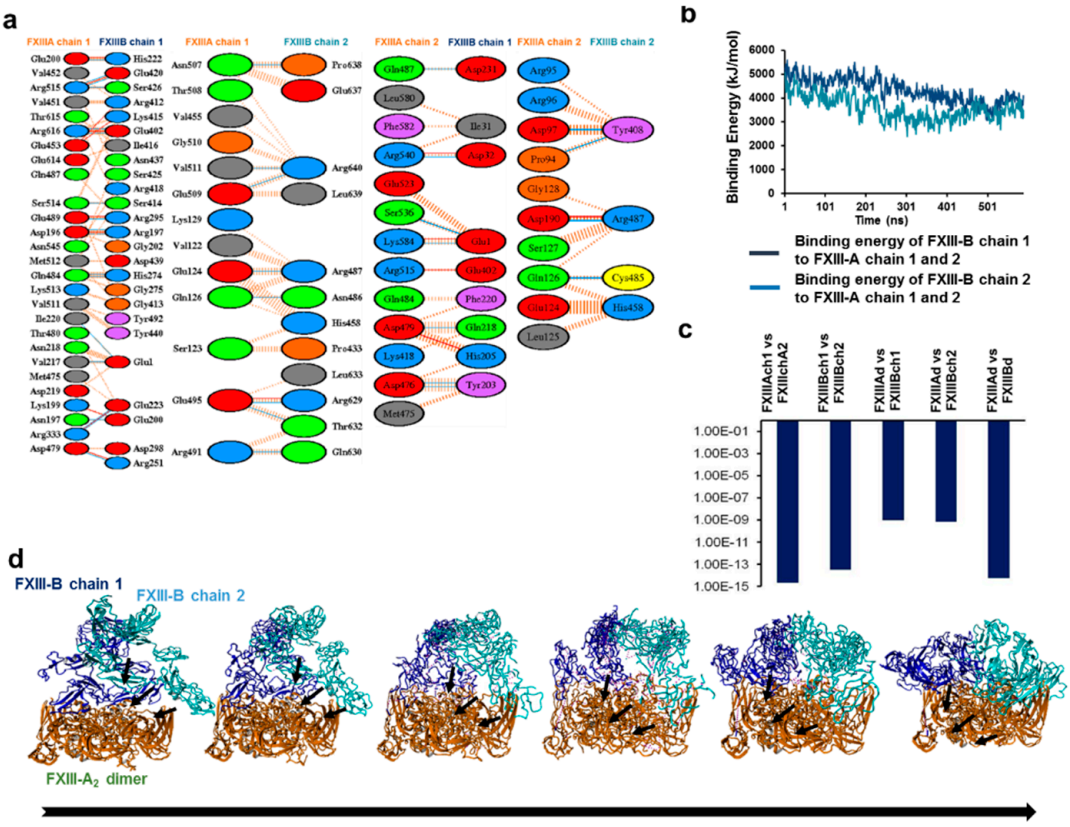

Figure 5. Interdomain interactions, binding affinity, and the assembly of the best FXIII-A_2B_2 complex model structure. (**a**) shows the different type of interactions between the different chains of FXIII-A and FXIII-B subunits within the best FXIII-A_2B_2 complex model structure. (**b**) shows a comparative binding energy graph of the two individual chains of the FXIII-B subunit to the FXIII-A_2 dimer as calculated during the MD simulation conducted in the best FXIII-A_2B_2 complex model structure. (**c**) show the comparative predicted binding affinities for different structural entities within the best FXIII-A_2B_2 complex model structure as calculated over the PRODIGY server [38]. These entities are abbreviated as: FXIII-Ach1/FXIII-Ach2, FXIII-A subunit chain 1 and 2; FXIII-Bch1/FXIII-Bch2, FXIII-B subunit chain 1 and chain 2; FXIII-Ad/FXIII-Bd, FXIII-A and FXIII-B subunit dimers, respectively. (**d**) shows the conformational transitions taking place in the FXIII-B dimer during its association with the FXIII-A_2 subunit dimer. Both the subunits are depicted in ribbon format. Solid arrows represent the conformations adopted by FXIII-B during its association. The FXIII-A_2 subunit dimer is colored orange, whereas the individual monomers of FXIII-B subunit dimer are colored blue and cyan, respectively.

3.6. Transition State Analysis Suggests Stepwise Binding Events during the Association of FXIII-A: FXIII-B Subunits

Since FXIII-A_2B_2 assembly occurs in plasma, we modeled the association events taking place during FXIII-A_2 and FXIII-B_2 interaction leading up to complex formation using transition state

analysis. The transition state analysis of the heterotetramer assembly shows that the association of dimeric subunits to form a complex is asymmetric, two-step binding, where FXIII-B monomer first strongly associates with FXIII-A_2 dimer, stabilizing a transient state FXIII-A_2B'B (where B' represents the unbound monomer). This complex then forms the FXIII-A_2B_2 complex where all subunits interact in totality (Figure 5d). These data show that the two-step asymmetrical binding most likely results in unequal pairing between the monomers within the complex.

3.7. Thermodynamic Patterns Underlying FXIII-A_2B_2 Complex Assembly and Dissociation Suggest Stepwise Models for Both Events

Finally, having investigated the complex assembly and disassembly (during activation) events at a structural level, we performed ITC for the same events to explain the operant thermodynamic variables. ITC enabled us to (a) examine the thermal changes corresponding to protein interface interactions upon binding and (b) correlate the thermal motions derived from activation-induced disassembly of the complex to the structural dynamics of individual subunits obtained by the model analyses. The first set of ITC experiments were performed to illustrate the thermal mechanics underlying the binding of FXIII subunits. When fitted with one set of binding sites, data measuring association of FXIII-A_2 and FXIII-B_2 yielded a K_d of 66.7 nM. A sequential two-step binding model based on hints from the unequally paired FXIII-A_2B_2 complex model 1 suggested that the first binding event of FXIII-B_2 to FXIII-A_2 is an enthalpically-favorable exothermic reaction ($\Delta H = -226.25$ kJ/mol), however, yields a conformationally-restricted state with positive, unfavorable entropy ($-T\Delta S > 0$) and K_d of 1.5 nM. The second binding event ($MA \leftrightarrow MA_2$) is also enthalpically favorable ($\Delta H = -360$ kJ/mol) with unfavorable entropic changes ($-T\Delta S > 0$), but a comparably weaker K_d of 4.3 μM, due to the spatial restriction faced by the second monomer upon interaction (Figure 6). These thermodynamic patterns agree with our transition state analysis suggesting a two-step binding assembly, the latter being of low affinity, leading to heterotetramer assembly.

To analyze the dissociation of the complex upon activation, we also interrogated calcium binding to the thrombin-cleaved FXIII-A_2B_2 complex. On the basis of the stoichiometric equilibrium model (Figure 7a) post-fitting, the first calcium binding event (set at K_d 100 μM [39–41]) showed an entropically-driven, negative -TΔS, and unfavorable, endothermic ΔH (4.78 kJ/mol) pattern. The second event, corresponding to K_d of 1 mM, had highly negative −TΔS, and endothermic ΔH (150.70 kJ/mol) behavior. In contrast, the third event, corresponding to K_d of 1.94 μM, had a highly positive −TΔS and exothermic ΔH (−154.42 kJ/mol) (Figure 7) heat change. Experiments assessing thrombin- and calcium-mediated dissociation of FXIII-A_2B_2 suggested the events proceeded stepwise. (i) Calcium binds to FXIII-A_2 in the heterotetramer complex. (ii) The calcium-bound heterodimer separates (i.e., FXIII-AB). Given heat signatures (Figure 7d) obtained for event 2 ($\Delta H > 0$, $-T\Delta S > 0$), we propose that the system maintains thermal equilibrium by first dissociating into a transient FXIII-AB heterodimer. This step combats the unfavorable enthalpy of A/A or B/B subunits suggested by the in silico pseudo-binding energy calculated for our complex model 1 (Figure 5c). (iii) The FXIII-AB heterodimer separates into individual, free subunits. During this event, unfavorable conformational entropies are counteracted by favorable enthalpic changes, which explain the final disruption of FXIII-AB heterodimer into calcium saturated, activated and open FXIII-A * monomer [31]). At the conditions used (T = 30 °C), all three events were spontaneous ($\Delta G < 0$). The flipping patterns of enthalpy and entropy in the sub-events that occur during dissociation of the complex suggests the role of bulk solvent coming into play, along with calcium saturation of FXIII-A that is responsible for stepwise disassembly of the complex [42–44]. Collectively, our thermodynamic data support the premise that FXIII undergoes two unique stepwise modes of complex assembly and disassembly in plasma (Supplementary Figure S11).

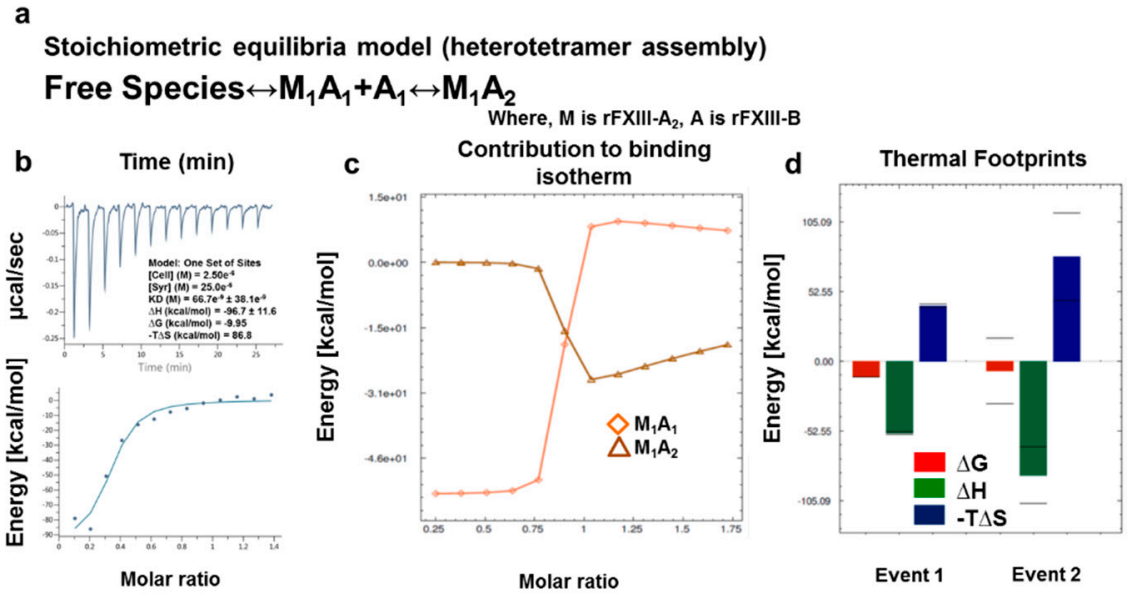

e

Event	K_d (nM)	ΔH (kJ/mol)
1. Free Species↔M_1A_1	1.5±0.04	-226.25±4.58
2. M_1A_1+A_1↔M_1A_2	4360±40.24	-360±8.96

Figure 6. In-solution associations of FXIII subunits studied by ITC. (**a**) is the equation depicting the stoichiometric binding equilibrium model, followed for the analysis of data derived from ITC (model was generated in Affinimeter using model builder approach). (**b**) represents the titration of 2.5 µM rFXIII-A_2 (in cell), with 25 µM FXIII-B subunits (in syringe). The upper image of this panel is the raw data depicting the heat change upon each injection; the lower image in this panel is the normalized data, with integrated heat change plotted against the concentration ratio of rFXIII-B vs. rFXIII-A_2. (blank controls not shown). A solid black line represents the corresponding fit obtained in Origin software using one-set of binding mode. (**c**,**d**) are based on Affinimeter analyses depicting the contribution of individual reactants of the equation (**a**) towards the isotherm. The heat signatures depicting the free energy changes, changes in enthalpy, and entropy in the two events explained in (**a**), respectively. (**e**) is a table explaining the two thermodynamic events, and their corresponding dissociation constants (K_d) and changes in enthalpy (ΔH).

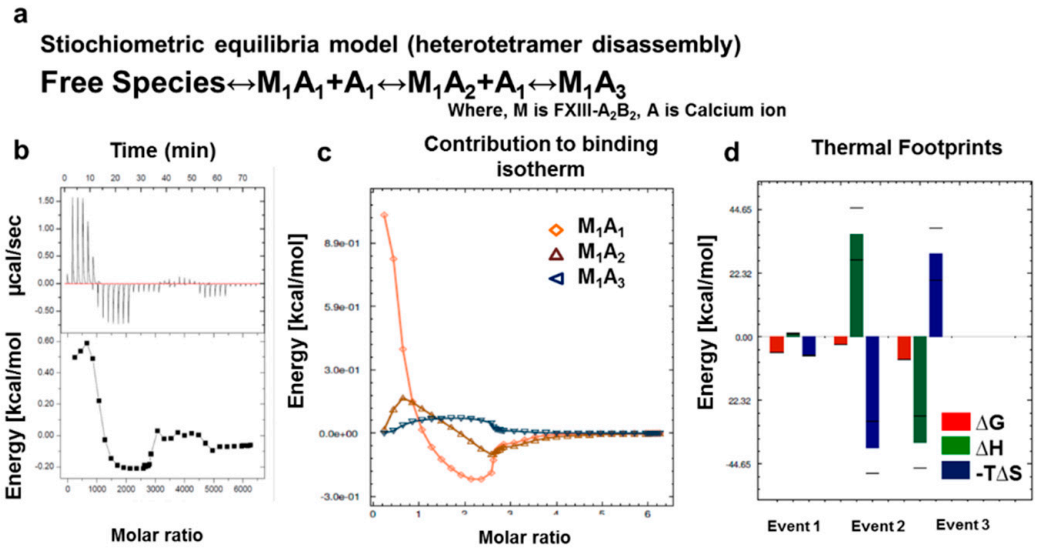

e

Event	K_d (µM)	ΔH (kJ/mol)
1. Free Species↔M_1A_1	100	4.78±6.1
2. M_1A_1+A_1↔M_1A_2	1000±0.0065	150.70±38.03
3. M_1A_2+A_1↔M_1A_3	1.94±0.86	-154.42±38.03

Figure 7. In-solution dissociation of FXIII complex in the presence of thrombin and calcium studied by ITC. (**a**) is the equation depicting the stoichiometric binding equilibrium model followed for the analysis of data derived from ITC (model was generated in Affinimeter using model builder approach). (**b**) represents the titration of 1.25 mM FXIII-A_2B_2, with 25 mM $CaCl_2$. Upper image of this panel is the ORIGIN raw data depicting the heat change upon each injection and the lower image in this panel is the normalized data, with integrated heat change plotted against the concentration ratio of $CaCl_2$ vs. FXIII. A solid black line represents the corresponding fit obtained in Origin software using one-set of binding mode. (blank controls not shown) (**c**,**d**) are based on Affinimeter analyses depicting the contribution of individual reactants of equation (**a**) towards the isotherm. The heat signatures depicting the free energy changes, changes in enthalpy, and entropy in the two events explained in Figure 6a, respectively. (**e**) is a table explaining the three thermodynamic events, and their corresponding dissociation constants (K_d) and changes in enthalpy (ΔH).

4. Discussion

4.1. IH Approaches Reveal a Unique FXIII Complex Structure

The FXIII complex has always presented a structural functional challenge to researchers owing to its dynamic nature and association with various other proteins such as fibrinogen in its physiological and biochemical life cycle. The interpretation of pathomolecular mechanisms is further limited by the absence of an all atom basis for this complex, as well as the development of drugs and inhibitors to bind both complexed and isolated FXIII-A [45–48]. Indirect evidence, in the context of interdomain interactions, exists but does not have a visual and structural basis [1]. The final structure of the FXIII-A_2B_2 complex model derived in this study fills this gap. Notably, our model presents a new picture of the complex that differs from the current paradigm in several important ways [1,6]. First, our model suggests FXIII-B subunit N-terminal sushi domains are relatively free, with positive surface electrostatic patches, indicating a potential role of this flexible region in interactions with other proteins like fibrinogen [30,31,33]. These interactions would be especially relevant when evaluating the effect of FXIII or fibrinogen surface mutations that disrupt or disorder their mutual complex. In addition, reports have suggested the N-terminal region of FXIII-B interacts with the

FXIII-A subunit [1]. This observation could also be a secondary allosteric effect observed during the competitive binding studies performed, since both our all-atom structure, as well as the XL-MS analysis, suggest increased density of interdomain interactions at the C-terminal end of FXIII-B. The recent report by Proptopopova et al. [49], based primarily on AFM studies in air, suggests partial wrapping of B subunits around central core of FXIII-A_2. Our study registers similar observations, but we propose a different orientation possibility for individual subunits within the complex. Differences between our interpretations might be due to the surface properties of the following: (a) complex; (b) the HOPG/mica surface; (c) sample preparation; or (d) imaging in air or buffer, which affects the overall behavior of the molecule under the microscope [32,50]. The association analyses by ITC reveal that the binding of individual subunits is strong (~10^{-9} M, single set of binding mode) but differs by a factor of 10 from the latest report (~10^{-10} M) in which one of the subunits was immobilized, unlike our solution-based label-free evaluation [1]. Interestingly, our heterotetramer model 2 generated from the flexible docking (which was observed to be stable over an MD simulation run for >100 ns) matches the previous literature on FXIII-A. The FXIII-B interactions, i.e., the C-terminal sushi domains of this model were observed to be free and the S1 and S2 sushi domains were observed to be partially interacting with the FXIII-B subunit (Supplementary Figure S9). Nevertheless, this model was eliminated from being the best representation, since it showed lower scores when matched to the AFM images of the heterotetramer (Figure 4). However, because of the similarity observed for the model 2 with previous literature, we do not completely deny that another conformational pose of the heterotetramer, one similar to the model 2, could actually be a more correct representative. Future studies involving cryo-EM-based exercises could shed more light in this regard.

4.2. Assembly of FXIII-A_2B_2 is a Two-Step Process Aided by the Conformational Flexibility of FXIII-B Subunit

Assembly of the FXIII-A_2B_2 complex in plasma and its subsequent activation and disassembly are well known phenomenon. However, the thermodynamic variables underlying these events have not been investigated in detail, especially in the context of the conformational changes that occur during these processes. Published data address only the thermolability of individual domains of FXIII-A subunit [51]. In contrast to transglutaminase-2 (TG2), a near homologue of FXIII-A which has been thoroughly investigated in the thermodynamic aspect [52], detailed data for the FXIII complex is not available. Our ITC experiments performed in-solution balance our structural investigation into FXIII oligomeric association and disassembly upon activation by identifying subtle changes in thermodynamic parameters that fit into our structural models. The thermodynamic study of FXIII complex assembly was performed by titrating both subunits against each other. Stepwise association of the two FXIII-B subunits onto FXIII-A dimer, also depicted by the in-silico transition state models, suggests the conformation adopted by the transient transition state FXIII-A_2BB' supports final complex association (Figure 5d). The heat signatures observed in our study show that desolvation of the inter-subunit interface leading to the stabilization of non-covalent contacts across the interface is a gradual two-step event aided by the conformational flexibility of FXIII-B subunits. While the globular FXIII-A structure remains relatively static, the flexible FXIII-B monomers twist and bend to individually accommodate the FXIII-A monomers. This two-step, unequal, asymmetrical assembly, further supported by the significantly different binding energies for the two events observed in our ITC profile (Figure 6), is the underlying cause for an unequally paired complex. This analysis is additionally supported by our AFM-based observations, in which the free form of FXIII-B is flexible and long but once associated with the FXIII-A, becomes more compact. Regardless of this association, even complex-bound FXIII-B retains some flexibility, especially at its N-terminal regions, as observed from the thermal motions of the complex model simulation (Supplementary video S1). These observations also suggest that the FXIII-B subunit undergoes a significant conformational change during its transition from a free molecule to a bound one.

4.3. Unequal Pairing within the FXIII Complex May Generate a Transient FXIII-AB Species during the Activation Induced Complex Disassembly

We studied FXIII complex disassembly by saturating thrombin-cleaved FXIII-A_2B_2 with increasing concentrations of calcium in an ITC platform. The thermodynamic driving forces responsible for complex activation indicate the role of solvation energies [43] that release the subunits in the presence of calcium ions (Figure 7). Here, the transition of the zymogenic heterotetramer to active, open, monomeric FXIII-A* involves formation of a transient FXIII-AB heterodimer in which FXIII-A subunits are incompletely saturated with calcium and are still loosely bound to one of the FXIII-B monomers. Our thermodynamic analyses indicate how low-entropy interfacial water molecules [42,53,54] assist in disrupting the tetrameric interface in FXIII-A_2B_2, aiding the entropic compensations that act against unfavorable enthalpies. The relevance of this model of dissociation becomes clearer when examining the nature of unequal pairing within the complex. Unequal pairing of individual FXIII-B monomers, especially at the C-terminal hinge region of FXIII-A (residues 500–520) (Supplementary Figure S12a, Supplementary videos S3 and S4), is favorable since it enables bulk solvent to sneak past the interface between loosely bound B monomer and A subunits (Supplementary Figure S12b), aiding dissociation to perform timed activation. This flexible hinge region is critical for the movement of FXIII-A barrel domains, enabling its activation and giving rise to its open extended conformation [8]. Equally strong binding of both FXIII-B subunit monomers to FXIII-A_2 would be energetically expensive, also yielding possibly slower activation and subunit dissociation. However, this observation does not suggest the complex breaks down into a trimer (FXIII-A_2B) and a monomer (FXIII-B), as is also observed in our SMD for separation of FXIII-B_2 from FXIII-A_2. Notably, bulk solvent and water does not play a role during the separation in the SMD (Supplementary video S2), unlike a physiological scenario in which it is an active participant. Bulk solvent/water permeates interfaces between all subunits, bringing a semblance of symmetry to the disruption and disassembly process in the physiological environment. Nevertheless, we can conclude that the process of dissociation is strong enough to separate FXIII-A monomers from each other (Supplementary video S2 and Supplementary Figure S13), providing further support that the activated FXIII-A molecule is a monomer [31]. Given the binding affinity of the FXIII subunits and their conformational motions, FXIII mutations that affect interface residues or conformational flexibility are likely to undermine complex assembly, resulting in either loosely or too tightly bound complex. A tightly bound complex can trap the oligomer in less flexible states and alter rates of activation, whereas a loosely held complex can be susceptible to spontaneous disassembly. The models of assembly and disassembly during activation of FXIII complex implicated by our study are particularly relevant in the context of the structural data and thermodynamics for research pharmacologists interested in generating inhibitors and drugs directed against the complex. The steps detailed in these events, especially in the thermodynamic context, can be objectively addressed to virtually and actually screen for inhibitors as has been done for TG2, FXIII's homologue [55].

4.4. Is Complex Interface a Potential Underlying Driver of Unexplained Heterozygous FXIII Mutations Observed in Mild FXIII Deficiency?

The catalytic FXIII-A subunit bears a special place in the transglutaminase (TGase) family as it is the only member that exists in a complexed form (FXIII-A_2B_2). Consequently, interfacial residues within the complex are under selective pressure, wherein mutations at these residues might be associated with a broad range of factor deficit (mild to severe FXIII deficiency). Inspection of recently reported missense mutations of F13A1 genes (p.His342Tyr, p.Asp405His, p.Gly411Cys, p.Gln416Arg, p.Leu539Pro, p.Arg540Gln, p.Gln601Lys, and p.Arg611His) [56–59] suggests these mutations lie on the interface rim [60] where they may be involved in FXIII-A and FXIII-B subunit interactions. Similarly, FXIII-B missense mutations (p.Cys336Phe, p.Val401Glu, p.Pro428Ser, and p.Cys430Phe) [61,62], also map to interfacial patches. Notably, a majority of these mutations were reported in the heterozygous state from mild FXIII deficiency patients. Since inherited FXIII deficiency is an autosomal recessive

disorder, the dominant negative effect of heterozygous FXIII gene mutations might be explained by their pathomolecular influence on the complex interface.

5. Conclusions

To summarize, our study presents not only a new view of the FXIII complex, but also proposes new mechanisms to explain FXIII complex association and disassembly. The structure provides a basis on which FXIII mutations (particularly those thought to affect the FXIII molecular interface) can be probed to define their pathomolecular mechanisms. Furthermore, our model provides the first atomic basis on which putative inhibitors can be designed and tested. Our models present interesting starting points for research into conformational changes occurring during FXIII complex assembly and disassembly. Further biochemical validation of hypotheses stemming from these models is warranted. In addition, the AFM-based analysis only presents a partial surface view of the structure, and therefore we plan to further refine the structure by matching it to cryo-EM based images of the $FXIIIA_2B_2$ complex.

Supplementary Materials: The following are available online at http://www.mdpi.com/2218-273X/9/12/765/s1.

Author Contributions: A.B. conceived and designed the project; S.S. performed the protein expression, purification, and ITC; A.N. performed and analyzed XL-MS; S.S. and S.K. performed AFM; J.-L.P. performed AFM dock analyses; A.B. performed all the in-silico analyses; S.S. and A.B. analyzed the data and co-wrote the manuscript; A.S.W., D.I., and J.O. read and edited the manuscript. All authors critically reviewed the manuscript.

Funding: This research was funded by the CSL Behring, grant number- N-045.0180.

Conflicts of Interest: Authors declare no conflict of interest.

References

1. Katona, E.; Pénzes, K.; Csapó, A.; Fazakas, F.; Udvardy, M.L.; Bagoly, Z.; Orosz, Z.Z.; Muszbek, L. Interaction of factor XIII subunits. *Blood* **2014**, *123*, 1757–1763. [CrossRef] [PubMed]
2. Radek, J.T.; Jeong, J.M.; Wilson, J.; Lorand, L. Association of the A subunits of recombinant placental factor XIII with the native carrier B subunits from human plasma. *Biochemistry* **1993**, *32*, 3527–3534. [CrossRef] [PubMed]
3. Biswas, A.; Ivaskevicius, V.; Thomas, A.; Oldenburg, J. Coagulation factor XIII deficiency. Diagnosis, prevalence and management of inherited and acquired forms. *Hamostaseologie* **2014**, *34*, 160–166. [CrossRef] [PubMed]
4. Stieler, M.; Weber, J.; Hils, M.; Kolb, P.; Heine, A.; Büchold, C.; Pasternack, R.; Klebe, G. Structure of active coagulation factor XIII triggered by calcium binding: Basis for the design of next-generation anticoagulants. *Angew. Chem. Int. Ed. Engl.* **2013**, *52*, 11930–11934. [CrossRef]
5. Fox, B.A.; Yee, V.C.; Pedersen, L.C.; Le Trong, I.; Bishop, P.D.; Stenkamp, R.E.; Teller, D.C. Identification of the calcium binding site and a novel ytterbium site in blood coagulation factor XIII by x-ray crystallography. *J. Biol. Chem.* **1999**, *274*, 4917–4923. [CrossRef]
6. Souri, M.; Kaetsu, H.; Ichinose, A. Sushi domains in the B subunit of factor XIII responsible for oligomer assembly. *Biochemistry* **2008**, *47*, 8656–8664. [CrossRef]
7. Seelig, G.F.; Folk, J.E. Noncatalytic subunits of human blood plasma coagulation factor XIII. Preparation and partial characterization of modified forms. *J. Biol. Chem.* **1980**, *255*, 8881–8886.
8. Gupta, S.; Biswas, A.; Akhter, M.S.; Krettler, C.; Reinhart, C.; Dodt, J.; Reuter, A.; Philippou, H.; Ivaskevicius, V.; Oldenburg, J. Revisiting the mechanism of coagulation factor XIII activation and regulation from a structure/functional perspective. *Sci. Rep.* **2016**, *6*, 30105. [CrossRef]
9. Bullock, J.M.A.; Sen, N.; Thalassinos, K.; Topf, M. Modeling Protein Complexes Using Restraints from Crosslinking Mass Spectrometry. *Structure* **2018**, *26*, 1015–1024. [CrossRef]
10. Zheng, J.; Corzo, C.; Chang, M.R.; Shang, J.; Lam, V.Q.; Brust, R.; Blayo, A.-L.; Bruning, J.B.; Kamenecka, T.M.; Kojetin, D.J.; et al. Chemical Crosslinking Mass Spectrometry Reveals the Conformational Landscape of the Activation Helix of PPARgamma; a Model for Ligand-Dependent Antagonism. *Structure* **2018**, *26*, 1431–1439.e6. [CrossRef]

11. Yang, L.; Yang, D.; de Graaf, C.; Moeller, A.; West, G.M.; Dharmarajan, V.; Wang, C.; Siu, F.Y.; Song, G.; Reedtz-Runge, S.; et al. Conformational states of the full-length glucagon receptor. *Nat. Commun.* **2015**, *6*, 7859. [CrossRef] [PubMed]
12. Zhang, X.; Wang, X.; Zhang, Z.; Cai, G. Structure and Functional Interactions of INO80 Actin/Arp Module. *J. Mol. Cell Biol.* **2018**. [CrossRef] [PubMed]
13. Chaves, R.C.; Dahmane, S.; Odorico, M.; Nicolaes, G.A.F.; Pellequer, J.-L. Factor Va alternative conformation reconstruction using atomic force microscopy. *Thromb. Haemost.* **2014**, *112*, 1167–1173. [CrossRef] [PubMed]
14. Doerr, A. A home for integrative structural models. *Nat. Methods* **2018**, *15*, 409. [CrossRef]
15. Burley, S.K.; Kurisu, G.; Markley, J.L.; Nakamura, H.; Velankar, S.; Berman, H.M.; Sali, A.; Schwede, T.; Trewhella, J. PDB-Dev: A Prototype System for Depositing Integrative/Hybrid Structural Models. *Structure* **2017**, *25*, 1317–1318. [CrossRef]
16. Thomas, A.; Biswas, A.; Ivaskevicius, V.; Oldenburg, J. Structural and functional influences of coagulation factor XIII subunit B heterozygous missense mutants. *Mol. Genet. Genom. Med.* **2015**, *3*, 258–271. [CrossRef]
17. Kaniyappan, S.; Chandupatla, R.R.; Mandelkow, E. Purification and Characterization of Low-n Tau Oligomers. *Methods Mol. Biol.* **2018**, *1779*, 99–111. [CrossRef]
18. Xu, D.; Jaroszewski, L.; Li, Z.; Godzik, A. AIDA: Ab initio domain assembly server. *Nucleic Acids Res.* **2014**, *42*, W308–W313. [CrossRef]
19. Yang, J.; Yan, R.; Roy, A.; Xu, D.; Poisson, J.; Zhang, Y. The I-TASSER Suite: Protein structure and function prediction. *Nat. Methods* **2015**, *12*, 7–8. [CrossRef]
20. Pierce, B.; Tong, W.; Weng, Z. M-ZDOCK: A grid-based approach for Cn symmetric multimer docking. *Bioinformatics* **2005**, *21*, 1472–1478. [CrossRef]
21. van Zundert, G.C.P.; Rodrigues, J.P.G.L.M.; Trellet, M.; Schmitz, C.; Kastritis, P.L.; Karaca, E.; Melquiond, A.S.J.; van Dijk, M.; de Vries, S.J.; Bonvin, A.M.J.J. The HADDOCK2.2 Web Server: User-Friendly Integrative Modeling of Biomolecular Complexes. *J. Mol. Biol.* **2016**, *428*, 720–725. [CrossRef]
22. Mattson, G.; Conklin, E.; Desai, S.; Nielander, G.; Savage, M.D.; Morgensen, S. A practical approach to crosslinking. *Mol. Biol. Rep.* **1993**, *17*, 167–183. [CrossRef]
23. Bonvin, A.M.J.J.; Karaca, E.; Kastritis, P.L.; Rodrigues, J.P.G.L.M. Defining distance restraints in HADDOCK. *Nat. Protoc.* **2018**, *13*, 1503. [CrossRef]
24. de Vries, S.J.; van Dijk, M.; Bonvin, A.M.J.J. The HADDOCK web server for data-driven biomolecular docking. *Nat. Protoc.* **2010**, *5*, 883–897. [CrossRef]
25. Krieger, E.; Vriend, G. YASARA View—Molecular graphics for all devices—From smartphones to workstations. *Bioinformatics* **2014**, *30*, 2981–2982. [CrossRef]
26. Krieger, E.; Koraimann, G.; Vriend, G. Increasing the precision of comparative models with YASARA NOVA–a self-parameterizing force field. *Proteins* **2002**, *47*, 393–402. [CrossRef]
27. Pierce, B.G.; Wiehe, K.; Hwang, H.; Kim, B.-H.; Vreven, T.; Weng, Z. ZDOCK server: Interactive docking prediction of protein-protein complexes and symmetric multimers. *Bioinformatics* **2014**, *30*, 1771–1773. [CrossRef]
28. Franklin, J.; Koehl, P.; Doniach, S.; Delarue, M. MinActionPath: Maximum likelihood trajectory for large-scale structural transitions in a coarse-grained locally harmonic energy landscape. *Nucleic Acids Res.* **2007**, *35*, W477–W482. [CrossRef]
29. Chaves, R.C.; Teulon, J.-M.; Odorico, M.; Parot, P.; Chen, S.-W.W.; Pellequer, J.-L. Conformational dynamics of individual antibodies using computational docking and AFM. *J. Mol. Recognit.* **2013**, *26*, 596–604. [CrossRef]
30. Chaves, R.C.; Pellequer, J.-L. DockAFM: Benchmarking protein structures by docking under AFM topographs. *Bioinformatics* **2013**, *29*, 3230–3231. [CrossRef]
31. Anokhin, B.A.; Stribinskis, V.; Dean, W.L.; Maurer, M.C. Activation of factor XIII is accompanied by a change in oligomerization state. *FEBS J.* **2017**, *284*, 3849–3861. [CrossRef] [PubMed]
32. Godon, C.; Teulon, J.-M.; Odorico, M.; Basset, C.; Meillan, M.; Vellutini, L.; Chen, S.-W.W.; Pellequer, J.-L. Conditions to minimize soft single biomolecule deformation when imaging with atomic force microscopy. *J. Struct. Biol.* **2017**, *197*, 322–329. [CrossRef] [PubMed]
33. Souri, M.; Osaki, T.; Ichinose, A. The Non-catalytic B Subunit of Coagulation Factor XIII Accelerates Fibrin Cross-linking. *J. Biol. Chem.* **2015**, *290*, 12027–12039. [CrossRef] [PubMed]

34. Byrnes, J.R.; Wilson, C.; Boutelle, A.M.; Brandner, C.B.; Flick, M.J.; Philippou, H.; Wolberg, A.S. The interaction between fibrinogen and zymogen FXIII-A2B2 is mediated by fibrinogen residues gamma390-396 and the FXIII-B subunits. *Blood* **2016**, *128*, 1969–1978. [CrossRef]
35. Kohler, H.P. Interaction between FXIII and fibrinogen. *Blood* **2013**, *121*, 1931–1932. [CrossRef] [PubMed]
36. Smith, K.A.; Pease, R.J.; Avery, C.A.; Brown, J.M.; Adamson, P.J.; Cooke, E.J.; Neergaard-Petersen, S.; Cordell, P.A.; Ariens, R.A.S.; Fishwick, C.W.G.; et al. The activation peptide cleft exposed by thrombin cleavage of FXIII-A(2) contains a recognition site for the fibrinogen alpha chain. *Blood* **2013**, *121*, 2117–2126. [CrossRef]
37. Wolberg, A.S. Fibrinogen and factor XIII: Newly recognized roles in venous thrombus formation and composition. *Curr. Opin. Hematol.* **2018**, *25*, 358–364. [CrossRef]
38. Xue, L.C.; Rodrigues, J.P.; Kastritis, P.L.; Bonvin, A.M.; Vangone, A. PRODIGY: A web server for predicting the binding affinity of protein-protein complexes. *Bioinformatics* **2016**, *32*, 3676–3678. [CrossRef]
39. Hitomi, K.; Kojima, S.; Fesus, L.; Máté, À. Demény, Ilma Korponay-Szabo, and Laszlo Fésüs. In *Chapter 1; Structure of Transglutaminases: Unique Features Serve Diverse Functions*; Hitomi, K., Kojima, S., Fesus, L., Eds.; Springer: Tokyo, Japan, 2015. [CrossRef]
40. Kristiansen, G.K.; Andersen, M.D. Reversible activation of cellular factor XIII by calcium. *J. Biol. Chem.* **2011**, *286*, 9833–9839. [CrossRef]
41. Ambrus, A.; Bányai, I.; Weiss, M.S.; Hilgenfeld, R.; Keresztessy, Z.; Muszbek, L.; Fésüs, L. Calcium binding of transglutaminases: A 43Ca NMR study combined with surface polarity analysis. *J. Biomol. Struct. Dyn.* **2001**, *19*, 59–74. [CrossRef]
42. Dragan, A.I.; Read, C.M.; Crane-Robinson, C. Enthalpy-entropy compensation: The role of solvation. *Eur. Biophys. J.* **2017**, *46*, 301–308. [CrossRef] [PubMed]
43. Olsson, T.S.G.; Ladbury, J.E.; Pitt, W.R.; Williams, M.A. Extent of enthalpy-entropy compensation in protein-ligand interactions. *Protein Sci.* **2011**, *20*, 1607–1618. [CrossRef] [PubMed]
44. Benfield, A.P.; Teresk, M.G.; Plake, H.R.; DeLorbe, J.E.; Millspaugh, L.E.; Martin, S.F. Ligand Preorganization May Be Accompanied by Entropic Penalties in Protein–Ligand Interactions. *Angew. Chem. Int. Ed.* **2006**, *45*, 6830–6835. [CrossRef] [PubMed]
45. Al-Horani, R.A.; Karuturi, R.; Lee, M.; Afosah, D.K.; Desai, U.R. Allosteric Inhibition of Factor XIIIa. Non-Saccharide Glycosaminoglycan Mimetics, but Not Glycosaminoglycans, Exhibit Promising Inhibition Profile. *PLoS ONE* **2016**, *11*, e0160189. [CrossRef]
46. Avery, C.A.; Pease, R.J.; Smith, K.; Boothby, M.; Buckley, H.M.; Grant, P.J.; Fishwick, C.W.G. (±) cis-Bisamido epoxides: A novel series of potent FXIII-A inhibitors. *Eur. J. Med. Chem.* **2015**, *98*, 49–53. [CrossRef]
47. Badarau, E.; Collighan, R.J.; Griffin, M. Recent advances in the development of tissue transglutaminase (TG2) inhibitors. *Amino Acids* **2013**, *44*, 119–127. [CrossRef]
48. Novakovic, J.; Wodzinska, J.; Tesoro, A.; Thiessen, J.J.; Spino, M. Pharmacokinetic studies of a novel 1,2,4-thiadiazole derivative, inhibitor of Factor XIIIa, in the rabbit by a validated HPLC method. *J. Pharm. Biomed. Anal.* **2005**, *38*, 293–297. [CrossRef]
49. Protopopova, A.D.; Ramirez, A.; Klinov, D.V.; Litvinov, R.I.; Weisel, J.W. Factor XIII topology: Organization of B subunits and changes with activation studied with single-molecule atomic force microscopy. *J. Thromb. Haemost.* **2019**, *17*, 737–748. [CrossRef]
50. Chang, C.-E.A.; McLaughlin, W.A.; Baron, R.; Wang, W.; McCammon, J.A. Entropic contributions and the influence of the hydrophobic environment in promiscuous protein-protein association. *Proc. Natl. Acad. Sci. USA* **2008**, *105*, 7456–7461. [CrossRef]
51. Kurochkin, I.V.; Procyk, R.; Bishop, P.D.; Yee, V.C.; Teller, D.C.; Ingham, K.C.; Medved, L.V. Domain structure, stability and domain-domaininteractions in recombinant factor XIII. *J. Mol. Biol.* **1995**, *248*, 414–430. [CrossRef]
52. Kanchan, K.; Ergülen, E.; Király, R.; Simon-Vecsei, Z.; Fuxreiter, M.; Fésüs, L. Identification of a specific one amino acid change in recombinant human transglutaminase 2 that regulates its activity and calcium sensitivity. *Biochem. J.* **2013**, *455*, 261–272. [CrossRef]
53. Gopal, S.M.; Klumpers, F.; Herrmann, C.; Schäfer, L.V. Solvent effects on ligand binding to a serine protease. *Phys. Chem. Chem. Phys.* **2017**, *19*, 10753–10766. [CrossRef]
54. Ben-Amotz, D. Water-Mediated Hydrophobic Interactions. *Annu. Rev. Phys. Chem.* **2016**, *67*, 617–638. [CrossRef]

55. Song, M.; Hwang, H.; Im, C.Y.; Kim, S.-Y. Recent Progress in the Development of Transglutaminase 2 (TGase2) Inhibitors. *J. Med. Chem.* **2017**, *60*, 554–567. [CrossRef]
56. Ivaškevičius, V.; Biswas, A.; Garly, M.-L.; Oldenburg, J. Comparison of F13A1 gene mutations in 73 patients treated with recombinant FXIII-A2. *Haemophilia* **2017**, *23*, e194–e203. [CrossRef]
57. Thomas, A.; Biswas, A.; Dodt, J.; Philippou, H.; Hethershaw, E.; Ensikat, H.J.; Ivaskevicius, V.; Oldenburg, J. Coagulation Factor XIIIA Subunit Missense Mutations Affect Structure and Function at the Various Steps of Factor XIII Action. *Hum. Mutat.* **2016**, *37*, 1030–1041. [CrossRef]
58. Biswas, A.; Ivaskevicius, V.; Thomas, A.; Varvenne, M.; Brand, B.; Rott, H.; Haussels, I.; Ruehl, H.; Scholz, U.; Klamroth, R.; et al. Eight novel F13A1 gene missense mutations in patients with mild FXIII deficiency: In silico analysis suggests changes in FXIII-A subunit structure/function. *Ann. Hematol.* **2014**, *93*, 1665–1676. [CrossRef]
59. Ivaskevicius, V.; Biswas, A.; Bevans, C.; Schroeder, V.; Kohler, H.P.; Rott, H.; Halimeh, S.; Petrides, P.E.; Lenk, H.; Krause, M.; et al. Identification of eight novel coagulation factor XIII subunit A mutations: Implied consequences for structure and function. *Haematologica* **2010**, *95*, 956–962. [CrossRef]
60. David, A.; Sternberg, M.J.E. The Contribution of Missense Mutations in Core and Rim Residues of Protein-Protein Interfaces to Human Disease. *J. Mol. Biol.* **2015**, *427*, 2886–2898. [CrossRef]
61. Ivaskevicius, V.; Biswas, A.; Loreth, R.; Schroeder, V.; Ohlenforst, S.; Rott, H.; Krause, M.; Kohler, H.-P.; Scharrer, I.; Oldenburg, J. Mutations affecting disulphide bonds contribute to a fairly common prevalence of F13B gene defects: Results of a genetic study in 14 families with factor XIII B deficiency. *Haemophilia* **2010**, *16*, 675–682. [CrossRef]
62. Hashiguchi, T.; Ichinose, A. Molecular and cellular basis of deficiency of the b subunit for factor XIII secondary to a Cys430-Phe mutation in the seventh Sushi domain. *J. Clin. Investig.* **1995**, *95*, 1002–1008. [CrossRef]